



Unveiling the stellar origin of the Wolf–Rayet nebula NGC 6888 through infrared observations

G. Rubio^{1,2}★ J. A. Toalá³ P. Jiménez-Hernández,³ G. Ramos-Larios^{1,2} M. A. Guerrero^{1,4}
V. M. A. Gómez-González,³ E. Santamaría^{1,2} and J. A. Quino-Mendoza^{1,2}

¹CUCEI, Universidad de Guadalajara, Blvd. Marcelino García Barragán 1421, 44430 Guadalajara, Mexico

²Instituto de Astronomía y Meteorología, Dpto. de Física, CUCEI, Av. Vallarta 2602, 44130 Guadalajara, Mexico

³Instituto de Radioastronomía y Astrofísica (IRyA), UNAM Campus Morelia, Apartado postal 3-72, 58090 Morelia, Mexico

⁴Instituto de Astrofísica de Andalucía, IAA-CSIC, Glorieta de la Astronomía s/n, E-18008, Granada, Spain

Accepted 2020 September 11. Received 2020 September 10; in original form 2020 July 17

ABSTRACT

We present a comprehensive infrared (IR) study of the iconic Wolf–Rayet (WR) wind-blown bubble NGC 6888 around WR 136. We use *Wide-field Infrared Survey Explorer*, *Spitzer* IRAC, and MIPS and *Herschel* PACS IR images to produce a sharp view of the distribution of dust around WR 136. We complement these IR photometric observations with *Spitzer* IRS spectra in the 5–38- μm wavelength range. The unprecedented high-resolution IR images allowed us to produce a clean spectral energy distribution, free of contamination from material along the line of sight, to model the properties of the dust in NGC 6888. We use the spectral synthesis code CLOUDY to produce a model for NGC 6888 that consistently reproduces its optical and IR properties. Our best model requires a double distribution with the inner shell composed only of gas, whilst the outer shell requires a mix of gas and dust. The dust consists of two populations of grain sizes, one with small-sized grains $a_{\text{small}} = [0.002–0.008] \mu\text{m}$ and another one with large-sized grains $a_{\text{big}} = [0.05–0.5] \mu\text{m}$. The population of big grains is similar to that reported for other red supergiants stars and dominates the total dust mass, which leads us to suggest that the current mass of NGC 6888 is purely due to material ejected from WR 136, with a negligible contribution of the swept up interstellar medium. The total mass of this model is $25.5^{+4.7}_{-2.8} \text{ M}_\odot$, a dust mass of $M_{\text{dust}} = 0.14^{+0.03}_{-0.01} \text{ M}_\odot$, for a dust-to-gas ratio of 5.6×10^{-3} . Accordingly, we suggest that the initial stellar mass of WR 136 was $\lesssim 50 \text{ M}_\odot$, consistent with current single stellar evolution models.

Key words: stars: evolution – stars: individual: NGC 6888, WR 136 – stars: winds, outflows – stars: Wolf–Rayet – infrared: ISM.

1 INTRODUCTION

Wolf–Rayet (WR) stars are formed as the result of the evolution of O-type stars with initial masses $> 20 \text{ M}_\odot$ (Ekström et al. 2012). The single stellar evolutionary scenario suggests that, before entering the WR phase, these stars become red supergiant (RSG) or luminous blue variable (LBV) stars whose slow winds ($v_\infty \approx 30–200 \text{ km s}^{-1}$) strip them from their hydrogen-rich outer layers producing dense structures around them (e.g. Cox et al. 2012; Morris et al. 2017). Furthermore, observational evidence suggests that the majority of massive stars are born in binary systems (Sana et al. 2012), which affect their evolution and, consequently, the production of WR stars (Mason et al. 2009; Eldridge et al. 2017). Mass transfer between the binary components or the ejection of a common envelope might also strip the hydrogen-rich envelope of one of the components creating a WR star (see e.g. Götzberg et al. 2018; Ivanova 2011, and references therein). Nevertheless, WR stars exhibit strong fast winds ($v_\infty \approx 1500 \text{ km s}^{-1}$, $\dot{M} \approx 10^{-5} \text{ M}_\odot \text{ yr}^{-1}$; Hamann, Gräfener & Liermann 2006) that sweep and compress the previously ejected material. This interaction produces a wind-blown bubble around the WR star and, at the

same time, the strong ultraviolet (UV) flux from the progenitor star ionizes the material (e.g. Garcia-Segura & Mac Low 1995). The combination of all these effects produces WR nebulae (see Chu 1981).

WR nebulae have radii as large as $\sim 10 \text{ pc}$ (e.g. Toalá et al. 2012, 2017) and in some cases exhibit multiple shells due to the eruptive mass ejection of the progenitor star (Marston 1995a; Marston et al. 1999). This demonstrates the powerful energy injection of very massive stars leveraging their role as one of the main actors shaping and enriching the interstellar medium (ISM). Spectroscopic studies of WR nebulae can unveil the production of heavy elements in their interiors, which can be used to test stellar evolution models and the chemical gradients in their host galaxies (Esteban et al. 2016; Méndez-Delgado et al. 2020). However, these structures are short-lived and therefore seldomly detected. WR nebulae will experience hydrodynamical instabilities causing them to break and to dissipate into the ISM within a few times 10^4 yr (Freyer, Hensler & Yorke 2006; Toalá & Arthur 2011). That is, not many WR stars exhibit associated nebulae (Gruendl et al. 2000; Stock & Barlow 2010), thus, producing detailed studies of known WR nebulae can bring us closer to understanding the violent impact of massive stars in the ISM.

Massive stars have been appointed to be laboratories for studying dust formation, processing and evolution (Verhoest et al. 2009;

* E-mail: grubio@idec.edu.mx

Gvaramadze, Kniazev & Fabrika 2010; Wachter et al. 2010). During the RSG and LBV phases, these stars reduce their effective temperature, $T_{\text{eff}} \lesssim 10^4$ K, allowing the formation of dust in their surroundings. The details of these processes depend on whether the star evolved through an RSG or LBV phase. RSG stars, with their enhanced mass-loss rates ($\dot{M} \lesssim 10^{-4} M_{\odot} \text{ yr}^{-1}$), may form dust-rich shells with dust sizes as large as a few times $0.1 \mu\text{m}$ (see Scicluna et al. 2015, and references therein). Meanwhile, the eruptive nature of the high mass-loss rate of LBV stars ($\dot{M} \gtrsim 10^{-3} M_{\odot} \text{ yr}^{-1}$; Weis 2001) may cause the dust to be shielded from stellar radiation, allowing it to grow to sizes as large as $1 \mu\text{m}$ (Kochanek 2011) as reported for the iconic LBV star η Car (Morris et al. 2017). Dust production can also occur at the interacting wind surface of massive binaries. In particular, carbon-rich WR stars (WC) with OB companions have been found to exhibit dust-rich pinwheel nebulae (e.g. Tuthill, Monnier & Danchi 1999; Marchenko et al. 2002). Furthermore, it has been suggested that dust can also form in the ejecta of a common-envelope phase around a binary system (Lü, Zhu & Podsiadlowski 2013).

Dust has been found spatially associated with the brightest optical regions of WR nebulae. Early infrared (IR) studies of WR nebulae showed that dust is thermally heated by the strong ionizing flux from their progenitor stars (van Buren & McCray 1988). Larger cavities harbouring WR nebulae have also been detected through IR and radio observations and these very likely correspond to the previous bubble carved by the feedback of the progenitor star during the main sequence phase (Marston 1995b, 1996; Arnal & Cappa 1996; Cappa et al. 1996). Marston (1991) presented the analysis of far-IR *IRAS* observations of the WR nebulae NGC 2359, RCW 58, and NGC 6888 and suggested that their dust masses were in the range of 0.25 – $1.3 M_{\odot}$. Taking into account the typically adopted dust-to-gas ratio of 0.01, the total nebular masses of these WR nebulae were too large to have a stellar origin. Accordingly, Marston (1991) attributed them to swept up material from the ISM. A subsequent study presented by Mathis et al. (1992) demonstrated that these mass estimates can change dramatically if the effects of the radiation field from the star are accounted for.

The advent of a new generation of IR satellites provided us with the opportunity of spatially resolve structures in WR nebulae, improving our understanding of dust processing in nebulae around massive stars (see Cichowolski et al. 2020). Furthermore, *Spitzer* and *WISE* have been used to unveil a new population of obscured nebulae around LBV and WR stars (Gvaramadze et al. 2010; Toalá et al. 2015). More recently, *Herschel* observations of M 1-67 around WR 124 were presented by Vamvatira-Nakou et al. (2016). Their radiative transfer model predicted a total nebular mass of $22 M_{\odot}$ with a dust mass of $0.26 M_{\odot}$. These authors predicted dust particles with sizes between 2 and $10 \mu\text{m}$ in M 1-67, but such large dust particles have never been reported in circumstellar nebulae.

We have started a series of works to analyse publicly available IR observations of WR nebulae using the photoionization code CLOUDY (Ferland et al. 2017) in conjunction with detailed synthetic WR spectra obtained from the state-of-the-art Potsdam Wolf-Rayet Models (PoWR) models (Hamann & Gräfener 2004).¹ Our most recent work on the WR nebula M 1-67 showed that there is no need for dust with sizes larger than $1 \mu\text{m}$ to reproduce the nebular and dust properties (Jiménez-Hernández, Arthur & Toalá 2020, hereinafter Paper I). By combining modern tools, we were able to conclude that the origin of M 1-67 might have been due to a common envelope

scenario, which makes this WR nebula the first evidence of such process in massive stars.

In this paper, we present our analysis of the WR nebula NGC 6888 (also known as the Crescent Nebula; see Fig. 1 top left-hand panel) around WR 136 (also known as HD 192163), one of the most studied galactic WR nebulae. H α narrow-band emission images show a filamentary and clumpy structure (Stock & Barlow 2010), which very likely formed as a result of hydrodynamical instabilities generated through the wind–wind interacting scenario (e.g. Garcia-Segura, Langer & Mac Low 1996; Toalá & Arthur 2011). An outer skin of [O III] emission encompassing the clumpy structure results from the shock of the expanding RSG material pushed by the WR wind (Gruendl et al. 2000; Moore, Hester & Scowen 2000). This [O III] shell also confines the adiabatically shocked, X-ray-emitting hot bubble (see Toalá et al. 2016, 2014; Wrigge et al. 2005, and references therein).

Several studies have addressed the physical properties of NGC 6888 and in general all these studies result in similar abundances (see Fernández-Martín et al. 2012; Reyes-Pérez et al. 2015; Esteban et al. 2016; Stock & Barlow 2014, and references therein). Fernández-Martín et al. (2012) suggested that NGC 6888 is mainly composed of three structures: (i) an ellipsoidal inner broken structure formed by shocked shells from the WR and RSG stages, (ii) an outer spherical shell presumably formed by the breaking of the main sequence (MS) bubble, and (iii) a faint structure around the nebula created by the interaction of the MS winds and the local ISM. Using the ionization code CLOUDY, Reyes-Pérez et al. (2015) concluded that NGC 6888 is chemically homogeneous and uniformly filled with low-density material, 1 cm^{-3} , in stark contrast to the obvious different morphological components and previous density estimates.

Here, we present a complete analysis of the IR emission of NGC 6888. We use images and spectra from *WISE*, *Spitzer*, and *Herschel* that cover the 3–160- μm wavelength range. The images are used to study the distribution of dust in NGC 6888 in comparison with optical images. The spectral energy distribution (SED) in the IR, in combination with publicly available estimates of the abundances and nebular properties, has been used to model the properties of the dust and ionized components of NGC 6888 with the ionization code CLOUDY. Our paper is organized as follows. The observations are presented in Section 2. The analyses of the images, the IR photometry, and the IR spectra are presented in Sections 3–5, respectively. Our models of NGC 6888 are presented in Section 6. Finally, the discussion and conclusions are presented in Sections 7 and 8.

2 OBSERVATIONS

2.1 IR images and spectra

All the IR observations used in this work have been obtained from the NASA/IPAC Infrared Science Archive.² Details of the observations such as the telescope, instrument, spectral band, observation date and principal investigator (PI) are listed in Table 1. Archival IR images of NGC 6888 were obtained from *WISE*, *Spitzer* IRAC & MIPS, and *Herschel* PACS observations.³ All available IR images are presented in Fig. 2.

The available *Spitzer* Infrared Spectrograph (IRS) observations of NGC 6888 were obtained in *stare* mode (Houck et al. 2004).

²<https://irsa.ipac.caltech.edu/frontpage/>

³The *Herschel* PACS observations were obtained in the framework of the Mass-loss of Evolved StarS (MESS) project (Groenewegen et al. 2011).

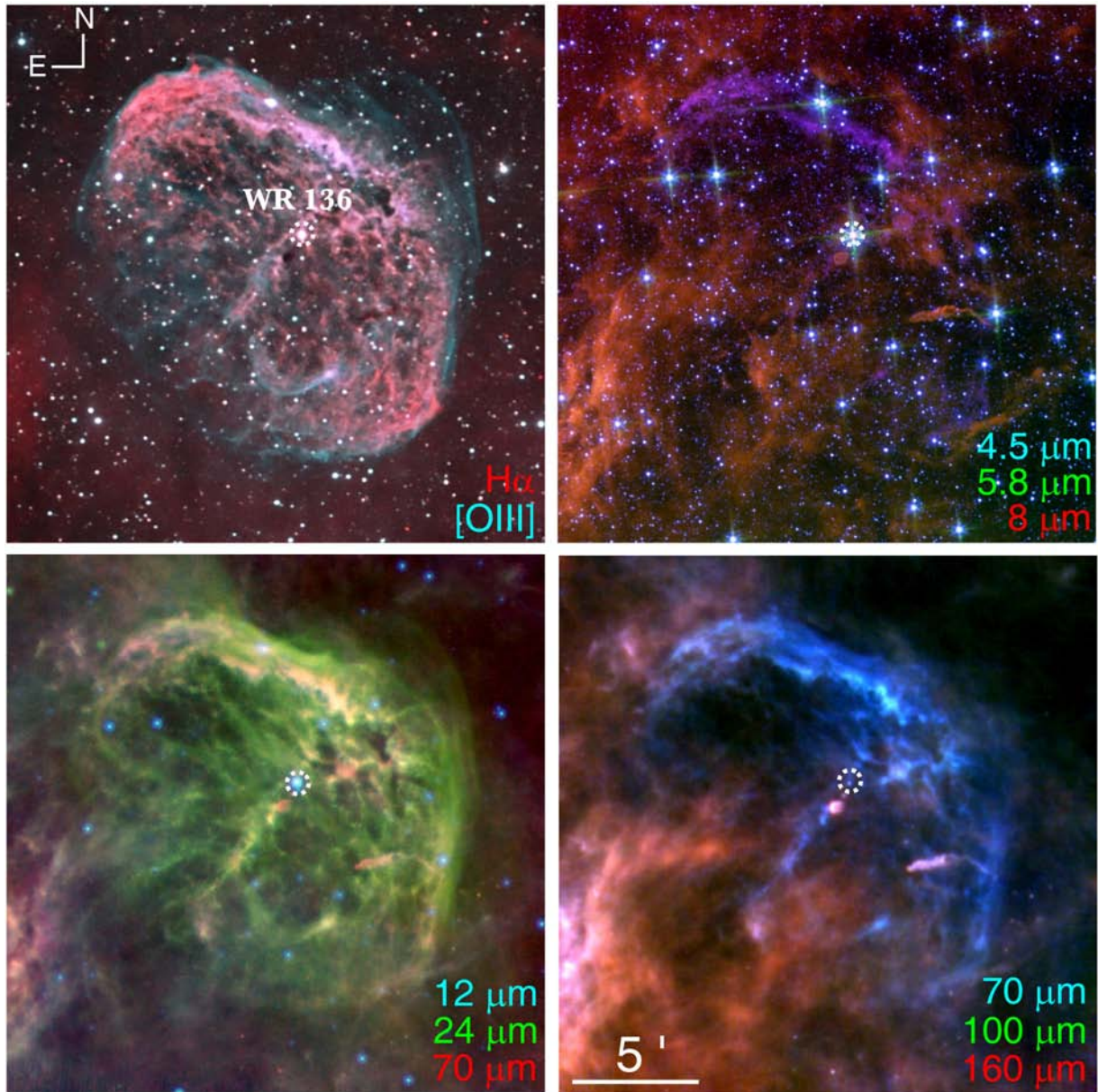


Figure 1. Optical and IR views of the WR nebula NGC 6888 showing different morphological structures and the spatial distribution of dust. Top left-hand panel: colour-composite optical image. Top right-hand panel: Composition of *Spitzer* IRAC images. Bottom left-hand panel: composition of different mid-IR instruments (*WISE*, *Spitzer* MIPS, and *Herschel* PACS). Bottom right-hand panel: composition of *Herschel* PACS images. The position of WR 136 is shown with a dashed-line circle. All panels have the same field of view.

Table 1. IR observations of NGC 6888 used in this work.

Telescope	Instrument	Band (μm)	Observations date (yyyy-mm-dd)	Observations ID	Processing level	PI
<i>Spitzer</i>	IRAC	3.6, 4.5, 5.8, 8.0	2005-10-21	20726	Level 2	J. Hester
	MIPS	24	2005-9-23	20726	Level 2	J. Hester
	IRS	SL (5–15), LL (14–39)	2006-11-9	30544	Level 2	P. Morris
<i>Herschel</i>	PACS	70, 160	2010-12-16	1342212042	Level 3	M. Groenewegen
		100, 160	2010-12-16	1342212040	Level 3	M. Groenewegen
<i>WISE</i>		12	2010-5-14	3031p378_ac51	Level 3	

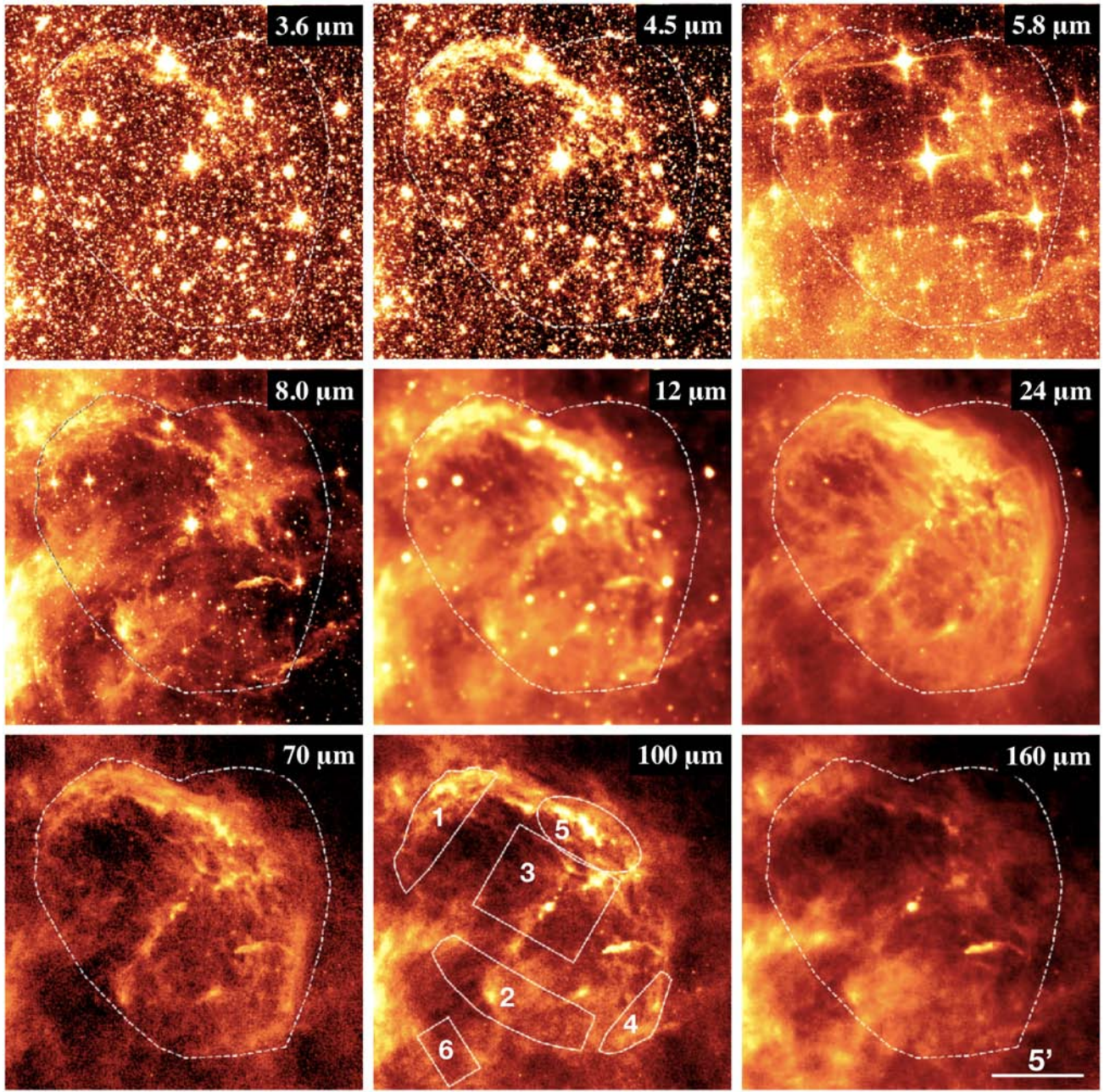


Figure 2. IR views of the WR nebula NGC 6888. Each panel corresponds to different IR filters (see Table 1). The dashed-line region delimits the optical [O III] emission detected in the optical (see Fig. 1). Regions labelled from 1 to 6 were used to derive the photometric measurements presented in Fig. 4. All panels have the same FoV as those in Fig. 1. North is up, east to the left.

These spectra were obtained with the low- and high-resolution modules, but unfortunately the high-resolution observations do not have suitable regions for background subtraction. Thus, we inspected these spectra, but no science was obtained from them. The low-resolution spectra correspond to the short-low (SL) and long-low (LL) modules covering the 5–38- μm wavelength range. The positions of the low-resolution slits are shown in Fig. 3.

The *Spitzer* IRS observations were analysed with the CUbe Builder for IRS Spectra Maps (CUBISM; Smith et al. 2007a) software. CUBISM tasks are used to combine spectra from the same position and to produce one-dimensional spectra. We followed the standard reduction

processes, which include background subtraction, characterization of noise in the data and bad pixel removal.

2.2 Optical imaging (OARP)

Optical narrow-band images of NGC 6888 were obtained at the Observatorio Astronómico Robótico Primavera (OARP) operated by the University of Guadalajara (Jalisco, Mexico). The facility is used by undergraduate, graduate, and doctoral programs in physics, astronomy, and astrophysics. Recently established, was strategically located just over 20 miles west of Guadalajara, where it was free from light pollution and clearer night sky. The observatory utilizes a 0.32m

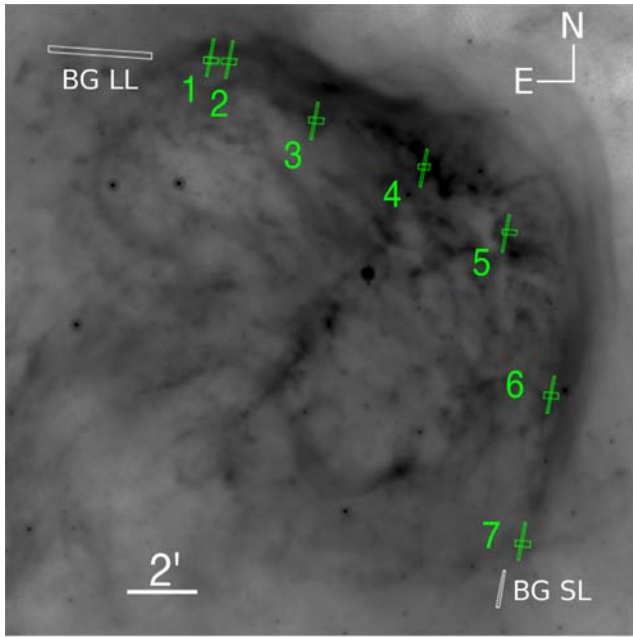


Figure 3. *Spitzer* MIPS 24- μm image of NGC 6888 showing the position of the SL and LL slits (green). The one oriented north to south corresponds to SL, the one oriented east to west is LL. The regions used to extract the background are shown with white rectangles.

f/8 CDK (Corrected Dall-Kirkham) telescope equipped with an SBIG STL-6303E/LE commercial camera, which uses a Kodak Enhanced KAF-6303E imaging sensor. This sensor consists of a 3072×2048 pixels array with a size of $9 \times 9 \mu\text{m}$ each. In combination with the telescope, it provides a field of view (FoV) of $37 \times 25 \text{ arcmin}^2$ and a plate scale of $0.73 \text{ arcsec pixel}^{-1}$.

Images of NGC 6888 were obtained on 2019 March 9 and 30 for total exposure times of 2 h in the [O III] filter and 1.5 h in the H α filter. These filters have central wavelengths and bandwidths of $\lambda_c = 6563 \text{ \AA}$ and $\Delta\lambda = 30 \text{ \AA}$, and $\lambda_c = 5007 \text{ \AA}$ and $\Delta\lambda = 30 \text{ \AA}$, respectively. The detector was set with a 2×2 binning. The data were bias-subtracted and flat-field corrected following standard Image Reduction and Analysis Facility (IRAF) routines (Tody 1993). A colour-composite optical image of NGC 6888 is presented in the top left-hand panel of Fig. 1.

3 DUST DISTRIBUTION

Fig. 2 presents the different IR images of NGC 6888 in the 3–160 μm wavelength range. All *Spitzer* IRAC images exhibit a large number of point sources in the vicinity of NGC 6888. The IRAC 3.6- and 4.5- μm images show a marginal detection coincident with the brightest optical regions of NGC 6888. Some emission is detected from the NE cap and in a lesser extent from the SW cap. No significant emission from the inner region is detected. The other two IRAC images, 5.8 and 8.0 μm , trace mostly clumps and filaments of the cold surrounding ISM.

The *Spitzer* MIPS image at 24 μm traces the continuum emission from dust present in the WR nebula (Toalá et al. 2015).

The *Herschel* PACS 70- μm image is very similar to that of the *Spitzer* MIPS, but the PACS 160- μm image rather traces the emission from the cold ISM. Meanwhile, the emission in the WISE 12 μm and *Herschel* PACS 100- μm images map the contribution from both the nebula and the ISM.

In general, most images presented in Fig. 2 trace the morphological features exhibited by the optical image of NGC 6888: the NE and SW caps and the NW blowout. The dark clump and filament described by Fernández-Martín et al. (2012) are clearly visible in the IRAC 5.8- and 8.0- μm images and in the *Herschel* images, they form part of the cold ISM. For a direct comparison with the optical image, we created three colour-composite IR pictures of NGC 6888 using (i) the 4.5-, 5.8-, and 8- μm *Spitzer* IRAC images, (ii) the 12-, 24- and 70- μm mid-IR images, and (iii) the 70, 100, and 160- μm *Herschel* PACS images. These three images are also presented in Fig. 1 along with the optical image of NGC 6888. These combinations of images exhibit in great detail the nebular and dust distribution of NGC 6888. The images confirm the suggestion of Toalá et al. (2014) that NGC 6888 is expanding towards a low-density region along the NW direction, which might be producing the expansion of the blowout. At the same time, the colour-composite IR pictures in Fig. 1 indicate that NGC 6888 is placed behind a molecular filament.

The colour-composite IR panels of Fig. 1 disclose an interesting feature. In the three IR panels, there is a dark region separating the contribution from NGC 6888 with that of the ISM. This effect is more clearly seen around the NE cap. The lack of IR emission is spatially coincident with the [O III] optical emission, which according with Gruendl et al. (2000) traces the expanding shock generated by the wind–wind interaction that created the WR nebula. The diminished IR emission in this layer suggests that dust is being destroyed by the expansion of the shock into the ISM. To further illustrate this, we present in Appendix A close up images of the NE cap of NGC 6888.

4 IR PHOTOMETRY

In order to produce a consistent model of the nebular and dust properties of NGC 6888, we extracted the IR photometry of each available image presented in Fig. 2 for $\lambda \geq 12 \mu\text{m}$. We did not use the *Spitzer* IRAC observations because they include the contribution from several nebular lines as well as possible low-ionization emission lines from the ISM. Moreover, the large number of background stars hampers an appropriate selection of the extraction region.

The photometry extraction procedure is described in Paper I. We define extraction regions where the integrated flux can be easily computed by adding all the pixels in the image. The contribution from background stars is excised and thus it is not taken into account for the flux estimate. A similar procedure would be performed for background regions, but it shall be noted that the ISM around NGC 6888 is not homogeneous as revealed by the IR images of NGC 6888 shown in the previous section. To minimize the impact of the spatially varying background, several background regions surrounding NGC 6888 were selected to compute the same number of background-subtracted fluxes. We emphasize that regions SE from NGC 6888 were discarded because they show the strongest contribution from the ISM according to Figs 1 and 2.

The resultant mean and standard deviation of the flux values are used as the flux and its uncertainty (σ_{back}), respectively. Nevertheless, a total error must be computed by adding other uncertainties such as that obtained from the calibration (σ_{cal}) which depends on each instrument. Thus, the total error can be calculated as

$$\sigma_{\text{tot}} = \sqrt{\sigma_{\text{back}}^2 + \sigma_{\text{cal}}^2}. \quad (1)$$

We first extracted the corresponding photometry from an aperture encompassing the emission from the [O III] line that defines the complete nebular extension of NGC 6888 (see Fig. 1). This aperture is shown as a white dashed-line region in most panels of Fig. 2. The

Table 2. IR fluxes of NGC 6888 extracted from different regions.

Instrument	λ_c (μm)	Complete (Jy)	Region 1 (Jy)	Region 2 (Jy)	Region 3 (Jy)	Region 4 (Jy)	Region 5 (Jy)	Region 6 (Jy)	NGC 6888 (Jy)
<i>WISE</i>	12	17.3 ± 6.3	1.6 ± 0.6	1.6 ± 0.8	1.7 ± 1.1	0.5 ± 0.3	1.9 ± 0.5	0.3 ± 0.2	9.8 ± 2.7
<i>Spitzer</i> MIPS	24	66.9 ± 11.4	3.7 ± 0.7	4.1 ± 1.0	10.9 ± 1.4	1.7 ± 0.3	10.2 ± 0.7	0.2 ± 0.3	53.6 ± 3.5
<i>Herschel</i> PACS	70	281.1 ± 107.2	32.9 ± 8.2	24.0 ± 12.2	51.0 ± 16.3	17.7 ± 3.8	57.7 ± 7.8	2.7 ± 3.4	302.5 ± 41.0
<i>Herschel</i> PACS	100	320.5 ± 187.9	47.3 ± 12.6	59.1 ± 18.5	59.8 ± 24.9	24.3 ± 5.8	61.1 ± 11.9	13.4 ± 5.0	320.5 ± 62.7
<i>Herschel</i> PACS	160	414.4 ± 220.0	47.5 ± 13.2	111.2 ± 19.4	73.3 ± 26.1	21.7 ± 6.1	26.8 ± 12.5	32.4 ± 5.3	140.8 ± 65.6

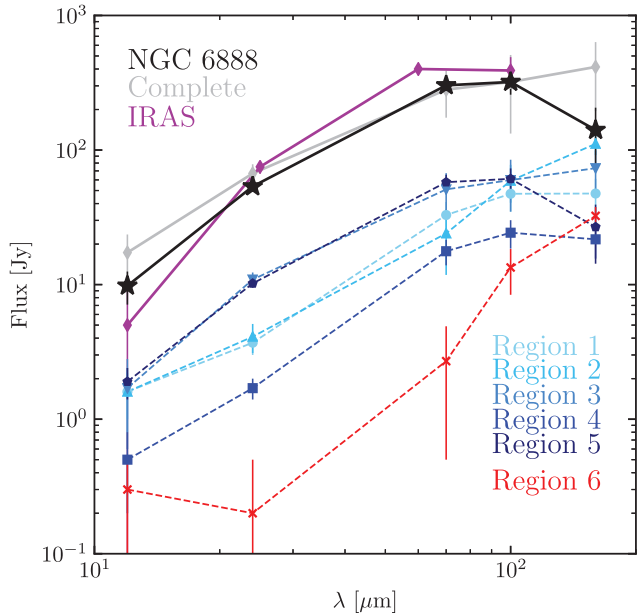


Figure 4. SED of the WR nebula NGC 6888 (stars) modelled in this paper. Different symbols (colours) show the SED of different regions in NGC 6888 as defined in the bottom-central panel of Fig. 2. The SED labelled as complete has been obtained taking into account the whole optical extension of the nebula. The purple SED labelled as IRAS is the photometry used by Mathis et al. (1992).

resultant flux and error values of this region are listed in Table 2 and illustrated in Fig. 4 as an SED labelled as Complete. Fig. 4 suggests that the Complete photometry of NGC 6888 peaks at wavelengths longer than 160 μm . However, as shown in Fig. 2 the dashed-line region includes a significant contribution (depending on the IR image) from gas that very likely has an ISM origin.

To assess the contribution from the ISM in the SED, we explored the variation of the IR SED from different regions within NGC 6888. The bottom central panel of Fig. 2 shows the different extraction regions here considered. Their corresponding photometry is listed in Table 2 and plotted and compared to the Complete SED in Fig. 4. This figure shows that the IR SED extracted from Regions 1–5 exhibit significant differences, but these can be explained by considering the SED of Region 6. The SED of this region, defined from an external filament to NGC 6888, increases with wavelength, suggesting the presence of colder dust in the ISM (see Section 6). Since the emission from NGC 6888 is projected against that of the ISM, this effect should also be present in other regions with different relative contributions. For example, the SED of Region 2, defined at the SE edge of NGC 6888, peaks at long wavelengths, i.e. it shows the noticeable contribution from the ISM as shown by Region 6.

An inspection of the SED from these different regions led us to conclude that Region 5 has an SED (mostly) free from the contribution from the ISM. Its SED has a peak located around ~ 70 – $100 \mu\text{m}$ consistent with the IR emission found in other WR nebulae. Assuming that the SED of Region 5 is thus representative of the shape of the SED of NGC 6888, its flux level has been normalized to that of the emission from the whole nebula to create an SED labelled as NGC 6888 that would describe our target. The resultant SED, which we will use to model the dust properties of NGC 6888, is presented in Fig. 4 and the corresponding flux values are listed in the last column of Table 2. For comparison, we also show in Fig. 4 the *IRAS* SED used in Mathis et al. (1992). The latter has larger fluxes at mostly all wavelengths except at 12 μm . The excess of the *IRAS* photometry compared to that estimated in this work is very likely due to the contribution from material in the line of sight and the point-like sources unresolved in the *IRAS* observations.

5 IR SPECTRA

Spitzer IRS spectra of NGC 6888 were extracted from the brightest regions following the N–NW–SW direction. The location of the extraction regions, as shown in Fig. 3, are labelled as Slit 1–7 and correspond to regions with the lowest or negligible contribution from the ISM. The spectra are very similar with a continuum from dust emission. The dominant emission lines in these spectra are those of [Ne II] 12.8 μm , [Ne III] 15.5 μm , [S III] 18.7 and 33.5 μm , [S IV] 10.5 μm , [Ar III] 8.98 μm , and [Si II] 34.8 μm (see Fig. 5). Other less intense lines correspond to He I at 22.9 μm and very likely an absorption due to N V at 29.5 μm . The latter implies the presence of gas with temperature around $\sim 10^5$ K at the mixing layer between the nebular cold ($\sim 10^4$ K) and the hot X-ray-emitting gas ($\sim 10^6$ K) filling NGC 6888 (e.g. Gruendl, Chu & Guerrero 2004; Fang et al. 2016). As an example, we show in Fig. 5 the spectrum from Slit 4 with the most prominent lines labelled.

The IRS spectra can be used to look for the presence of molecules in NGC 6888 such as H₂ and polycyclic aromatic hydrocarbons (PAHs) similarly to other nebulae around evolved stars such as planetary nebulae (see e.g. Mata et al. 2016; Fang et al. 2018; Toalá et al. 2019, and references therein) and, according to St-Louis et al. (1998), the interstellar nebula around WR 7 (NGC 2359). PAH features appear in the spectra of NGC 6888, but, after subtracting the background spectra, these disappear as illustrated in the middle panel of Fig. 5 showing the spectral range including the 7.7-, 8.6-, and 11.3- μm PAH features. Furthermore, no H₂ lines are detected in the IRS spectra of NGC 6888.

We used the PAHFIT routines (Smith et al. 2007b) to measure the line intensities and errors for each line for all seven spectra. The ions, flux, and errors of the most prominent lines are listed in Table 3. This table shows clear variations in the measured lines from slit to slit. In particular, emission lines from the Spectrum 4 exhibit the largest fluxes. We attribute these differences to the variations of the physical

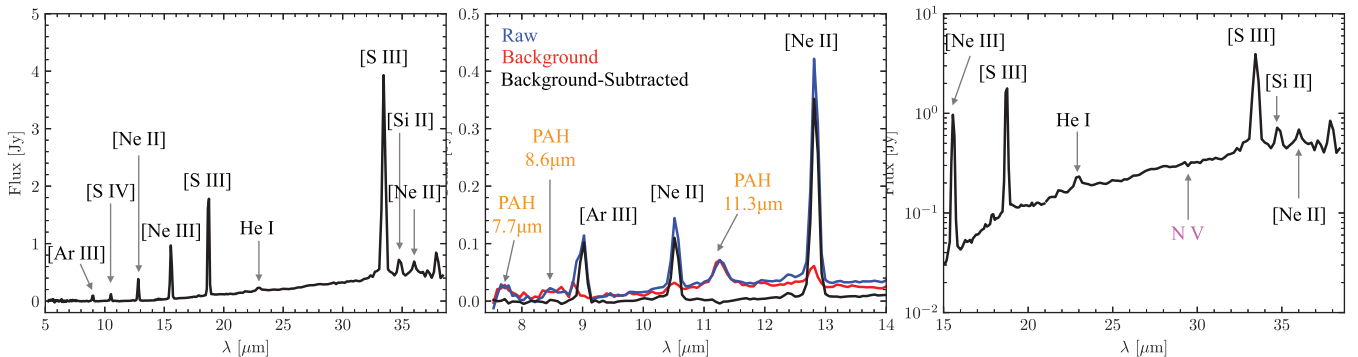


Figure 5. Background-subtracted low-resolution IRS spectra (black lines) extracted from Slit 4 as shown in Fig. 3. The most prominent lines are labelled. The left-hand panel shows the complete range of the low-resolution spectra while the other two shown different regions of the spectra. The middle panel also shows the background and background unsubtracted (raw) spectra.

Table 3. Fluxes of the emission lines detected in the *Spitzer* IRS observations of NGC 6888. Labels from 1 to 7 represent the extraction regions defined in Fig. 3.

Line	λ (μm)	1	2	3	Flux (mJy)	4	5	6	7	Model (mJy)
[Ar III]	8.98	1.1 ± 0.2	2.3 ± 0.8	6.7 ± 4.8	8.0 ± 2.1	3.9 ± 3.3	0.5 ± 1.9	0.3 ± 1.1		1.9
[S IV]	10.5	0.2 ± 0.05	0.7 ± 0.3	5.6 ± 3.9	8.4 ± 2.2	3.1 ± 2.7	0.4 ± 1.6	0.1 ± 0.5		2.2
[Ne II]	12.8	5.2 ± 0.1	4.3 ± 0.5	5.4 ± 1.4	6.1 ± 0.7	3.3 ± 1.4	0.9 ± 0.9	1.3 ± 1.0		1.4
[Ne III]	15.5	2.9 ± 0.004	3.1 ± 0.04	6.4 ± 0.05	10.8 ± 0.03	3.0 ± 0.005	1.2 ± 0.03	1.0 ± 0.05		2.5
[S III]	18.7	8.6 ± 0.01	9.3 ± 0.2	12.4 ± 0.2	17.4 ± 0.08	5.7 ± 0.01	2.1 ± 0.09	2.8 ± 0.3		9.3
[S III]	33.5	19.1 ± 0.02	20.2 ± 0.04	26.1 ± 0.04	34.9 ± 0.05	13.0 ± 0.03	5.8 ± 0.03	6.7 ± 0.05		22.6
[Si II]	34.8	2.9 ± 0.02	2.4 ± 0.02	2.8 ± 0.02	2.9 ± 0.03	1.8 ± 0.02	1.4 ± 0.02	1.8 ± 0.02		7.8
$n_e(\text{[S III]})$	(cm^{-3})	420	440	470	520	400	230	350		340

properties within the slit positions, e.g. due to the clumpy distribution of gas in NGC 6888. To corroborate this, we have computed the electron densities (n_e) using the [S III] 18.7 and 33.5 μm with PYNEB (Luridiana, Morisset & Shaw 2015). The $n_e(\text{[S III]})$ values are listed in the bottom row of Table 3 for each slit position and, indeed, show that Slit 4 has the largest density estimate.

6 DUST MODELLING

As a first approximation to the dust temperature (T_{dust}) and mass (M_{dust}), we fitted a modified blackbody (MBB) model to the IR SED of NGC 6888 with $\lambda \geq 70 \mu\text{m}$. Under the assumption that dust is optically thin and that all the dust has a single temperature, the MBB can be expressed as

$$F_\nu = \kappa_{v_0} \left(\frac{\nu}{\nu_0} \right)^\beta M_{\text{dust}} \frac{B_\nu(T_{\text{dust}})}{d^2}, \quad (2)$$

where $B_\nu(T_{\text{dust}})$ is the Planck function and κ_{v_0} is the dust emissivity adopted to be $\kappa_{v_0} = 27.1 \text{ g cm}^{-2}$ at the reference wavelength $\lambda = 100 \mu\text{m}$ (Draine 2003). We fitted the *Herschel* photometry taking β , T_{dust} , and M_{dust} as free parameters. The best fit that minimizes χ^2 corresponds to $\beta = 2.7 \pm 0.6$, $T_{\text{dust}} = 29.3 \pm 0.3 \text{ K}$, and $M_{\text{dust}} = 0.69 \pm 0.04 \text{ M}_\odot$. Similar temperatures for WR nebulae have been previously estimated with *IRAS* observations (e.g. Marston 1991). However, there is a known degeneracy between β and T_{dust} (Juvela et al. 2013) and thus, we computed another model by fixing $\beta = 2$ that resulted in $T_{\text{dust}} = 34.4 \pm 0.8 \text{ K}$ and $M_{\text{dust}} = 0.32 \pm 0.04 \text{ M}_\odot$. We note that the MBB fits are not meant to reproduce the complete IR photometry of NGC 6888, but they can be useful to estimate the

temperature of the large grain population, another constrain to our detailed model. Nevertheless, these approximations reveal that the dust grains must be present in a wide range of sizes and temperatures. These two MBB models are plotted in Fig. 6 in comparison with the observed IR SED. To further illustrate the differences with the physical properties of the material in the surrounding ISM, we also estimated the dust temperature for the photometry extracted for Region 6 (see Figs 2 and 4) probing this is ISM. The dust temperature for this emission is lower, $T_{\text{ISM}} = 16.7 \pm 0.4 \text{ K}$, as expected for cold ISM dust (see Ostrovskii et al. 2020, and references therein).

Our goal is to produce a characterization of the dust properties in NGC 6888 consistent with the nebular optical properties. For this, we used the spectral synthesis and plasma simulation code CLOUDY (version 17.01; Ferland et al. 2017) coupled with the PYCLOUDY libraries (Morisset 2013). The input parameters required by CLOUDY are (i) the form of the incident spectrum (a model of the spectrum of WR 136), (ii) the density distribution, (iii) abundances, and (iv) the dust properties (chemical composition and size distribution).

With these, CLOUDY is able to produce an emission model which is subsequently processed with the help of PYCLOUDY to create synthetic optical long-slit observations. Furthermore, synthetic IR SED photometry is produced by using the transmission curves from the different IR instruments used here.⁴ The synthetic observations are

⁴The transmission curves of the *WISE*, *Spitzer*, and *Herschel* instruments were obtained from <http://svo2.cab.inta-csic.es/theory/fps/index.php?mode=brwse>.

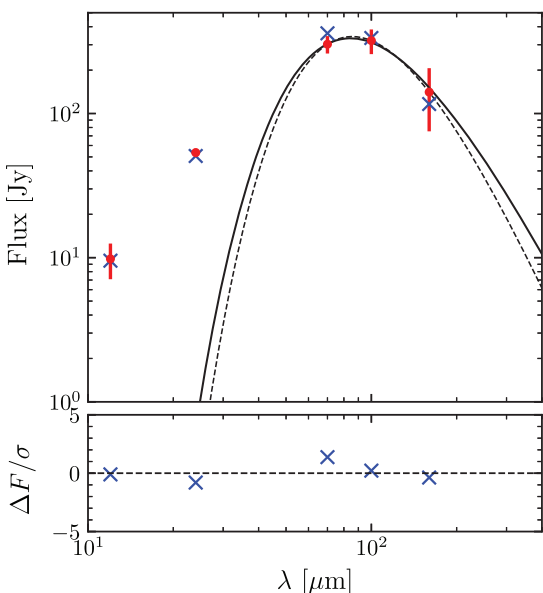


Figure 6. Observed IR SED of NGC 6888 (red dots) compared to the synthetic IR SED of our best fit model (blue crosses). The solid and dashed lines correspond to a MBB model with fixed $\beta = 2$ ($T_{\text{dust}} = 34.4 \pm 0.8$ K) and an MBB model with β as a free parameter ($\beta = 2.7 \pm 0.6$, $T_{\text{dust}} = 29.3 \pm 0.3$ K), respectively. The bottom panel shows the residuals between the observed and synthetic IR SED.

Table 4. Elemental abundances of NGC 6888 in units of $12 + \log(\text{X/H})$ reported for the slit A6 in Esteban et al. (2016) (hereafter, E16), Mesa-Delgado et al. (2014) (hereafter, MD14), and those used by Reyes-Pérez et al. (2015) (RP2015). The last column shows the abundances adopted for our model.

Element	E2016	MD2014	RP2015	Model
He	11.23 ± 0.06	11.21 ± 0.03	11.21	11.23
O	8.19 ± 0.13	8.20 ± 0.09	8.20	8.05
C	–	8.86 ± 0.31	8.86	8.86
N	8.27 ± 0.18	8.54 ± 0.20	8.40	8.68
Ne	7.51 ± 0.78	7.51 ± 0.20	7.51	7.78
S	6.92 ± 0.21	6.77 ± 0.20	7.10	6.92
Cl	4.99 ± 0.15	–	–	4.84
Ar	6.41 ± 0.11	6.41 ± 0.11	6.41	6.41

then compared to previously published optical studies of NGC 6888 and the IR observations (spectra and IR SED) presented in the previous sections to assess the validity of our models.

We started our modelling adopting the most recent abundances determinations reported by Esteban et al. (2016), which correspond to 10-m Gran Telescopio de Canarias OSIRIS spectroscopic observations. Their slit A6 is placed on a region spatially coincident with the one used here to estimate the total IR photometry of NGC 6888 (see fig. 1 in Esteban et al. 2016). Their abundances and emission-line fluxes obtained from these observations are listed in Tables 4 and 5, respectively. The total $H\beta$ flux [$F(H\beta)$] in logarithmic scale, the electron temperature (T_e), and n_e obtained from the [O III] and [S II] lines, respectively, are also presented in the bottom rows of Table 5. We note that during the fitting process, some of the abundances had to be tuned in order to reproduce simultaneously the optical and IR emission lines. For comparison, we also show in Table 4 the abundances reported by other works.

Table 5. Emission lines for region A6 of NGC 6888 in E16 compared to the predictions from our model. All line fluxes are normalized with respect to $H\beta = 100$.

Line	λ (Å)	E16 (Slit A6)	Model
[O II]	3726	50.4 ± 4.7	39.4
[O III]	4363	1.4 ± 0.4	1.5
He I	4471	8.8 ± 0.4	8.1
[O III]	4959	81.3 ± 1.7	82.1
[O III]	5007	242.9 ± 4.9	245.1
[Cl III]	5518	0.5 ± 0.1	0.6
[Cl III]	5538	0.4 ± 0.1	0.4
[N II]	5755	1.3 ± 0.1	2.2
He I	5876	25.8 ± 0.7	23.6
[N II]	6548	41.8 ± 1.2	51.0
$H\alpha$	6563	301.6 ± 9.0	286.8
[N II]	6583	130.3 ± 3.9	150.3
He I	6678	7.0 ± 0.4	5.9
[S II]	6716	5.1 ± 0.3	4.4
[S II]	6731	4.2 ± 0.3	3.6
He I	7065	4.2 ± 0.5	4.2
[Ar III]	7136	15.2 ± 0.7	26.1
$c(H\beta)$		0.62 ± 0.03	0.65
$\log(F(H\beta))$	(erg s $^{-1}$ cm $^{-2}$)	-13.01 ± 0.01	-13.01
n_e ([S II])	(cm $^{-3}$)	200 ± 140	198
T_e ([O III])	(K)	9550 ± 820	9708

Table 6. Principal stellar parameters of WR 136.

d (kpc)	$1.9^{+0.14}_{-0.12}$	Bailer-Jones et al. (2018)
WR-subtype	WN6h	Hamann et al. (2019)
M_* (M_\odot)	23/21	Hamann et al. (2019)
$\log(L)$ (L_\odot)	5.78	Hamann et al. (2019)
T_* (kK)	70.8	Hamann et al. (2019)

We demonstrated in Paper I that a detailed prescription of the stellar atmosphere is necessary to obtain a more realistic description of the nebular and dust parameters. The progenitor star of NGC 6888, WR 136, has been modelled by Hamann et al. (2019) using the updated version of the stellar atmosphere code PoWR. The best-fitting stellar parameters reported in that work are listed in Table 6. Accordingly, we retrieved the model labelled as WNL 10–16 with Galactic metallicity and hydrogen fraction of 0.2 from the PoWR database. This model is presented in Fig. 7 compared to a blackbody emission model with the same effective temperature (70 kK) as well as the stellar model used by R15 kindly provided by J. Reyes-Pérez. In the following, we will adopt the distance of $d = 1.9^{+0.14}_{-0.12}$ kpc estimated by Bailer-Jones et al. (2018) using the *Gaia* data release.

6.1 Detailed modelling of NGC 6888

The $H\alpha$ and [N II] images of NGC 6888 show an apparent elliptical shape with semimajor and semiminor axes of 540 and 360 arcsec, respectively. At a distance of 1.9 kpc, the physical size of NGC 6888 is 5 pc and 3.9 pc, respectively. Marston & Meaburn (1988) showed, however, that the kinematics of NGC 6888 can be broadly fit by an expanding spherical shell with an expansion velocity of 85 km s $^{-1}$, although we note that a shell with blisters would be more accurate as unveiled by the [O III] image. For this, we adopted a spherically symmetric shell for our model. An averaged angular radius of 450 arcsec was set as a fixed parameter for the outer radius (r_{out}).

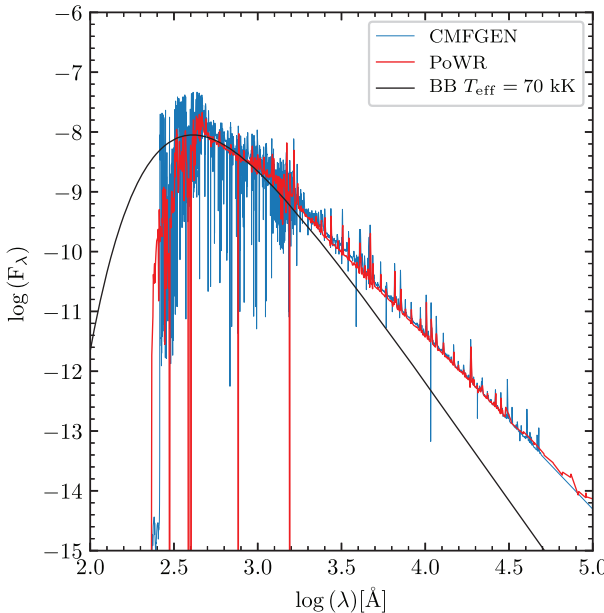


Figure 7. Comparison between different stellar atmosphere models. The blue line corresponds to the stellar atmosphere from CMFGEN used in RP15 while the red line is the PoWR model used in this work. The black line presents a blackbody emission model with an effective temperature of 70 kK.

The inner radius (r_{in}) was varied along with the filling factor (ϵ) and n_e to try to fit the optical observations and physical properties of NGC 6888. Values between $n_e \lesssim 100\text{--}500 \text{ cm}^{-3}$ for the electron density have been reported in the literature (Esteban & Vilchez 1992; Fernández-Martín et al. 2012; Esteban et al. 2016, see also Table 3), but we note that it is very likely that the largest values correspond to dense clumps detected in H α and [N II] narrow-band images (see Fig. 1).

We performed a large number of models fixing r_{out} but varying r_{in} for families of n_e values. None of these models resulted in good nebular parameters comparable to those reported for NGC 6888. Consequently, we followed the results from RP15 and considered two shells: an inner shell with density n_1 between r_{in} and r_{mid} and a filling factor ϵ_1 composed purely of gas, and an outer shell with density n_2 between r_{mid} and r_{out} and ϵ_2 . The outer shell includes contributions from both gas and dust. A schematic view of this model is presented in Fig. 8.

Our best model that reproduces the nebular properties of NGC 6888 was achieved with $n_1 = 400 \text{ cm}^{-3}$, $n_2 = 180 \text{ cm}^{-3}$, $\epsilon_1 = 10^{-3}$, and $\epsilon_2 = 0.07$. The radii are $r_{\text{in}} = 400 \text{ arcsec}$, $r_{\text{mid}} = 425 \text{ arcsec}$, and $r_{\text{out}} = 450 \text{ arcsec}$. The synthetic intensities of the most important optical lines are listed in Table 5 in comparison with those reported in E16 for their slit A6. The emission IR lines obtained from our model are compared to those obtained from the *Spitzer* IRS observations in Table 3. Despite the variations obtained from the *Spitzer* IRS spectra, the model broadly reproduces the IR lines, corroborating previous findings that suggest that the inner regions of NGC 6888 are dominated by photoionization (Esteban & Vilchez 1992; Esteban et al. 1993; RP15). Although we note that there might be certain components associated to shocks which produce line excitation (Gruendl et al. 2000; Moore et al. 2000)

As noted before, we started our fitting process by adopting the set of abundances reported for slit A6 by E16. However, some elemental abundances required small changes in order to fit both the optical and IR emission lines. Nevertheless, most of them resulted in values

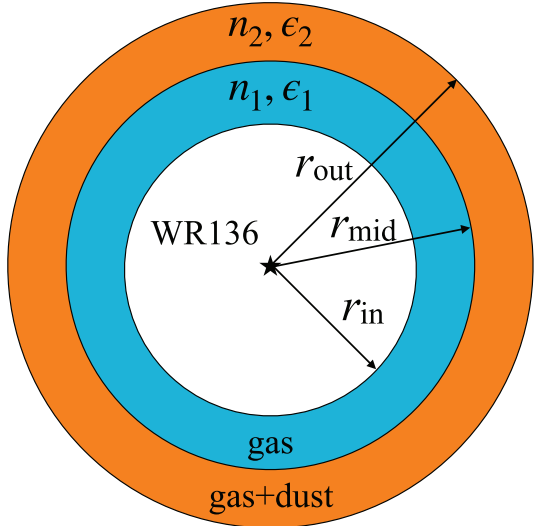


Figure 8. Schematic view of the two-shell density distribution used to model the nebular and IR properties of NGC 6888. The outer shell accounts for the presence of gas and dust while the inner shell only contains gas.

close to those reported in the literature. In particular, the O abundance had to be reduced to 8.05, a small value compared to what has been reported by the references in Table 4, but marginally similar to the lower value reported by E16. The last column in Table 4 lists the final abundances used for our best model.

Once we have modelled the observed emission lines of NGC 6888, we now include dust in our calculations to produce synthetic IR photometry. During the RSG and LBV phase, massive stars are copious producers of oxygen, which condense molecules, such as silicates in their atmospheres (Verhoelst et al. 2009; Dharmawardena et al. 2020). Accordingly, we adopt grains composed of amorphous astronomical silicate. In particular, Cloudy includes olivine (MgFeSiO_4) as the default silicate grain.

Initially, we used two distribution of dust sizes as those used in Mathis et al. (1992): a distribution for small grains with sizes $a_{\text{small}} = [0.002\text{--}0.008] \mu\text{m}$ and another for big grains with sizes $a_{\text{big}} = [0.005\text{--}0.25] \mu\text{m}$. However, our first attempts to model the IR SED suggested the need of extending the size of the large grains. Finally, we found that a population of sizes for the big grains of $a_{\text{big}} = [0.05\text{--}0.50] \mu\text{m}$ improved our model. The maximum size of the big grains was fixed to $0.50 \mu\text{m}$ as found for the RSG star VY Canis Majoris (Scicluna et al. 2015). In all cases, the grains are spherical and their sizes follow a Mathis, Rumpl & Nordsieck (1977) power-law distribution $\propto a^{-3.5}$ with 10 size bins for each distribution.

To reproduce the observed IR SED, our model requires a large amount of big grains, with a big grains-to-small grains ratio of 16:1 and a resultant dust-to-gas ratio of 5.6×10^{-3} . The synthetic photometry obtained from our model is compared to the observed IR SED in Fig. 6. Our best model suggests that the total mass of NGC 6888 is $25.5^{+4.7}_{-2.8} M_{\odot}$ with a total dust mass of $M_{\text{dust}} = 0.14^{+0.03}_{-0.01} M_{\odot}$, less than a half of that estimated by the MBB model with fixed $\beta = 2$. The model predicts a mass for the big grains of $0.134^{+0.03}_{-0.01} M_{\odot}$. We note that the errors in the total mass and dust mass estimates were obtained by propagating the errors in the distance as reported by Bailer-Jones et al. (2018).

In Fig. 9, we show the temperature distribution for different bin sizes of the dust grains located in the outer shell. The temperature

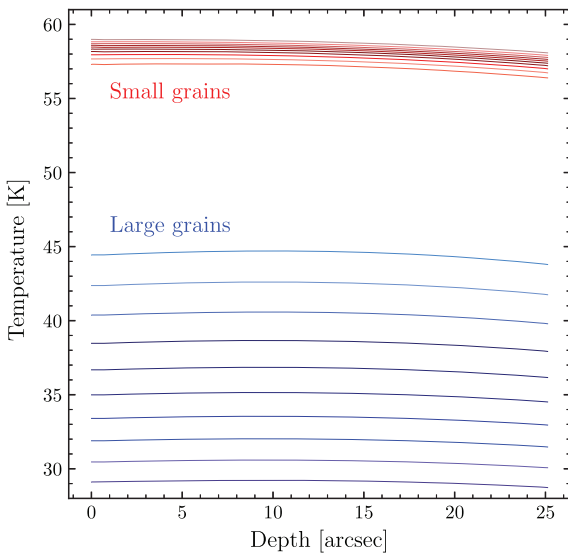


Figure 9. Temperature distribution for the different dust sizes used for our best model of NGC 6888. Each line represents a size bin of the small ($a_{\text{small}} = [0.002\text{--}0.008] \mu\text{m}$) and large grains ($a_{\text{big}} = [0.05\text{--}0.5] \mu\text{m}$).

for the large grains is in the range estimated using the MBB approximation.

7 DISCUSSION

7.1 On the spatial distribution of dust in NGC 6888

Our analysis above has disclosed an unprecedented view of the IR emission of the WR nebula NGC 6888. The *Herschel* PACS and *Spitzer* IRAC images have revealed in great detail the distribution of dust in this WR nebula and the ISM around it. These are shown in the colour-composite IR panels of Fig. 1, which are compared to the optical image of NGC 6888. Such detailed morphological IR characteristics of NGC 6888 are only allowed by the spatial resolution of the observations used here as compared with the *IRAS* images used in previous analyses (Marston 1991; Mathis et al. 1992).

An interesting feature seen in the IR panels in Fig. 1 is a gap between the dust in NGC 6888 and the emission that traces the outer cold dust from the ISM. This situation is clearly seen in the NE cap of NGC 6888 and to a lesser extent towards the SW cap. For example, Fig. 1 bottom right-hand panel shows a dark region separating the *Herschel* images at 70 and 160 μm . A careful comparison between the [O III] and IR images of the nebula shows that the former is distributed exactly in the dark region observed in the colour-composite IR panels of this figure (see Appendix A).

Gruendl et al. (2000) presented the analysis of H α and [O III] narrow-band images of a sample of eight bright WR nebulae, including NGC 6888. They showed that the [O III] emission is smooth and traces the leading shock of the expanding nebula, while the H α emission displays a clumpy morphology trailing inside the [O III] emission (see Fig. 1 top left-hand panel). Gruendl et al. (2000) argued that the displacement between these two emission lines is due to radiative cooling. Behind the shock front, the temperature drops while the density increases displacing the two emissions. We suggest that this dark region, which is coincident with the [O III] leading shock, is unveiling the destruction of dust at the edge of NGC 6888.

The destruction of dust grains may be due to thermal evaporation, gas–grain collisions and destruction by grain–grain collisions (see Woitke, Dominik & Sedlmayr 1993). According to Jones, Tielens & Hollenbach (1996) the destruction of silicate dust grains in low-velocity shocks can be attributed to non-thermal sputtering while large grains ($\sim 0.1 \mu\text{m}$) are easily shattered in grain–grain collisions. Slavin, Jones & Tielens (2004) presented calculations on the dust–gas decoupling on dust destruction in shocks. They found that grains with a large range of sizes are almost completely destroyed by shock waves with velocities around $75\text{--}150 \text{ km s}^{-1}$. The reported expansion velocity of NGC 6888, $\sim 80 \text{ km s}^{-1}$ (Chu, Treffers & Kwitter 1983; Marston & Meaburn 1988), makes plausible the destruction of dust at the edge of NGC 6888 as the nebula expands.

7.2 Consequences of the dust model

Taking advantage of an improved analysis of the spatial distribution of dust in NGC 6888, we managed to uncover its true IR SED. This represents an improvement over the nebular estimates made from low-resolution *IRAS* observations. Our best model is able to reproduce nebular optical and IR properties of NGC 6888 using an appropriate description of the stellar atmosphere of WR 136. This resulted in a total mass of NGC 6888 of $25.5^{+4.7}_{-2.8} M_\odot$ with a dust-to-gas ratio of 5.6×10^{-3} , that is, a total dust mass of $M_{\text{dust}} = 0.14^{+0.03}_{-0.01} M_\odot$. If we assume a duration of $2 \times 10^5 \text{ yr}$ for the RSG phase, we can estimate an averaged mass-loss rate of $(1.28^{+0.23}_{-0.15}) \times 10^{-4} M_\odot \text{ yr}^{-1}$, consistent with that expected for the RSG phase.

Our results represent an improvement to the work of Mathis et al. (1992). They tried to fit simultaneously the nebular properties and the low-spatial resolution *IRAS* observations of NGC 6888. We have shown that their SED overestimated the real IR flux from this WR nebula. Although the estimated mass is of the same order as that estimated by our model ($20 M_\odot$), they used a blackbody model for the stellar radiation field with $T_{\text{eff}} = 50 \text{ kK}$. These authors restricted the large size of their big grains to $0.25 \mu\text{m}$ but we found that increasing it to $0.5 \mu\text{m}$ improved significantly our comparison with the IR SED. The limit of $0.5 \mu\text{m}$ was set following the findings of Scicluna et al. (2015) on the RSG VY Canis Majoris. We note that a smaller population of big grains did not result in a good fit to the IR SED. In addition, we tried models with dust sizes larger than $0.5 \mu\text{m}$ without significant improvement. It is important to note that 93 per cent of the dust mass corresponds to grains with sizes similar to those obtained for RSG stars (larger than those estimated for the ISM). That is, we are detecting the material ejected in the previous RSG phase with negligible contribution from swept up ISM material.

It seems indeed that the total mass of the nebula corresponds to material ejected by WR 136 in its previous RSG phase without any contribution from swept-up ISM material as suggested by the analysis of the IR images. Adopting a current mass for WR 136 of $\sim 22 M_\odot$ (see Table 5; Hamann et al. 2019) one can estimate its initial mass to be $\lesssim 50 M_\odot$. This is corroborated by the stellar evolutionary models presented by Ekström et al. (2012).⁵ In Fig. 10, we present HR diagrams obtained by using stellar evolution models at $Z = 0.014$ with and without rotation with initial masses between 32 and $60 M_\odot$. The stellar parameters (T_{eff} and L) estimated from the PoWR stellar atmosphere models (Hamann et al. 2019) are somewhat consistent with WR 136 having an initial mass of $50 M_\odot$. Abundance estimates, in particular, the He versus C/O diagram presented by E16, are also

⁵The models were retrieved from the Geneva Code webpage: <https://www.unige.ch/sciences/astro/evolution/en/database/>.

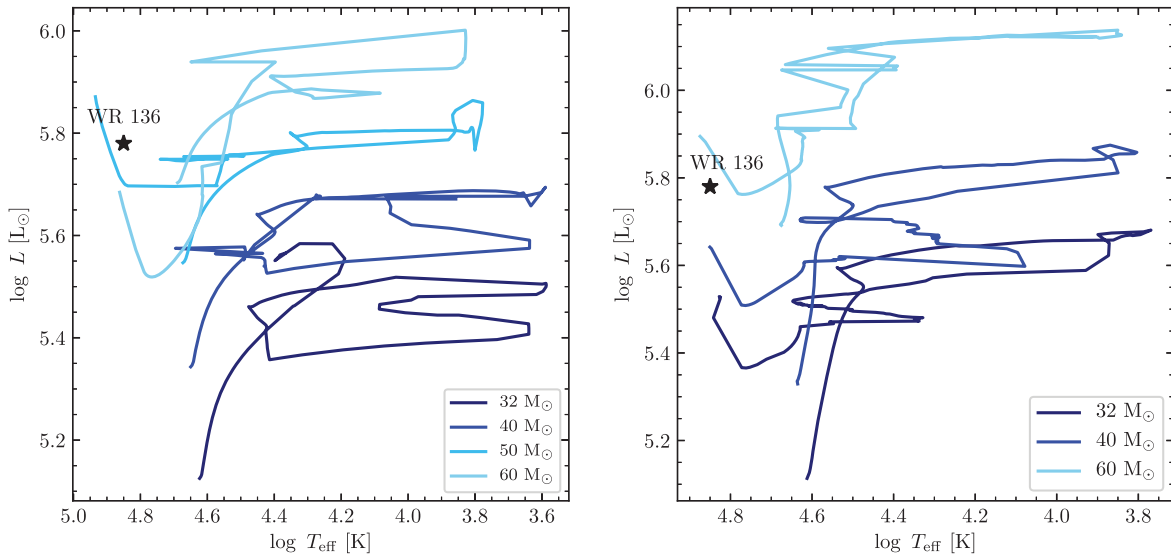


Figure 10. Hertzsprung–Russell diagrams of stellar evolution models with initial masses between 30 and 60 M_{\odot} from Ekström et al. (2012). The black star represents the position of WR 136. Different colours represent models from different initial masses. The left- (right-hand) panel presents model without (with) stellar rotation. There is no star model available with initial mass of 50 M_{\odot} in the Geneva Code web page.

consistent with this finding (see fig. 9 in that paper). Finally, we calculated the averaged mass-loss rate predicted for a 50 M_{\odot} stellar evolution model. This resulted in $1.9 \times 10^{-4} M_{\odot}$, very similar to that estimated using our detailed model.

We note that other authors have estimated ionized masses of $\sim 4 M_{\odot}$ (see Wendker et al. 1975; Kwitter 1981; Marston & Meaburn 1988) for NGC 6888 using radio and H α line emission. We have recalculated their estimates by following the procedure in Marston & Meaburn (1988) using the H α intensity with the current distance of 1.9 kpc and an electron density of 180 cm $^{-3}$ as obtained for the dominant shell in our model (also consistent with observations). This resulted in $21.9^{+7.2}_{-5.0} M_{\odot}$, which is consistent with the total estimated mass from our Cloudy model, but slightly smaller. This seems to suggest that NGC 6888 is almost completely ionized. If the difference, $3.6 M_{\odot}$, is considered to be neutral material, this should be shielded from the UV radiation from WR 136 in the dense clumps and filaments seen in the H α + [N II] images.

It is not necessary to invoke a contribution from the ISM in the mass of NGC 6888. An appropriate distance estimation by means of the *Gaia* observations, and improvement of the stellar evolution models, and a careful dissection of the IR SED have allowed us to conclude that the origin of this WR nebula is purely due to processed ejected stellar wind.

We would like to point out that in order to produce a consistent model of WR nebulae one must take into account important aspects such as an appropriate description of the WR stellar atmosphere of the progenitor star and the simultaneous treatment of gas and dust (see Paper I). In particular, we note here that the density distribution of our model was initially based on the findings reported by RP15 which only modelled the photoionized structure of NGC 6888.

Although these authors used a very similar WR stellar atmosphere as that used in this work (see Fig. 7), the inclusion of dust in the model requires some tuning to the density parameters to simultaneously fit the optical and IR observations.

Finally, we note that our model predictions have been compared to single stellar evolution models, but it is currently accepted that massive stars are born in binary systems affecting their evolution (see

Section 1). However, there is no observational evidence that WR 136 is a binary star (see Gräfener et al. 2012; Fullard et al. 2020) and the clumpy morphology of its associated WR nebula seems to have been the result of instabilities produced by the wind–wind interaction scenario, in contrast to the ballistic expanding clumps expected in a common envelope stripping scenario (see discussion in Paper I).

8 CONCLUSIONS

We presented a characterization of the distribution and properties of dust in the WR nebula NGC 6888 around WR 136. We used archival IR observations (spectra and images) that cover the 3–160- μm wavelength range in conjunction with the photoionization code CLOUDY to model simultaneously the properties of the ionized and dust components in NGC 6888. Our findings can be summarized as follows:

(i) The combination of the IR images allowed us to perform an unprecedented study of the spatial distribution of dust in NGC 6888. The high-resolution IR images used here helped us to dissect the contribution from dust in NGC 6888 and that corresponding to the ISM. We discovered a dark region between the IR emission at the outer edge of the WR nebula coincident with the [O III] optical emission. We suggest that this dark region is unveiling the destruction of dust at the edge of NGC 6888 due to its relatively high expansion velocity ($\sim 80 \text{ km s}^{-1}$).

(ii) The IR photometry extracted taking into account the nebular morphology of NGC 6888 is heavily contaminated by the contribution from ISM clouds and filaments, a problem that could not be properly resolved in previous IR studies of this WR nebula. By studying the IR SED from different regions within NGC 6888 and its immediate surroundings, we suggest that the NW region has no contamination from the ISM. The true IR SED of NGC 6888 peaks between 70 and 100 μm , very similar to other WR nebulae.

(iii) Our best model to the nebular parameters and IR SED was achieved by adopting a spherical two-shell distribution with inner and outer densities of $n_1 = 400 \text{ cm}^{-3}$ and $n_2 = 180 \text{ cm}^{-3}$ and filling

factors of 10^{-3} and 0.07, respectively. We adopted two population of dust grains with sizes $a_{\text{small}} = [0.002\text{--}0.008] \mu\text{m}$ and $a_{\text{big}} = [0.05\text{--}0.50] \mu\text{m}$, the later in line with the large dust grains in the RSG star VY Canis Majoris. The total dust mass in NGC 6888 resulted in $0.14^{+0.03}_{-0.01} M_{\odot}$ with a dust-to-gas ratio of 5.6×10^{-3} . The small grains contribute to 6 per cent of the total dust mass.

(iv) We found that the dust in NGC 6888 is dominated by large dust with RSG origin, which suggests that this WR nebula is mainly composed by material ejected by the star with negligible contribution from swept up ISM.

(v) The total estimated mass of NGC 6888 is $25.5^{+4.7}_{-2.8} M_{\odot}$, together with the estimates from Hamann et al. (2019) for its progenitor star, leads us to suggest an initial mass $\lesssim 50 M_{\odot}$ for WR 136. This result is supported by stellar evolution models, in particular, the prediction of the mass-loss rate and the abundance determinations reported in the literature.

ACKNOWLEDGEMENTS

The authors would like to thank the referee, Anthony P. Marston, for comments and suggestions that improved the presentation of this paper. The authors are also thankful to J. Reyes-Pérez for providing the CMFGEN model of WR 136. GR would like to thank S.J. Arthur and people at IRyA-UNAM for their support during the realization of this project. GR, ES and JAQ-M acknowledge support from Consejo Nacional de Ciencia y Tecnología (CONACyT) for student scholarship. JAT, GR, and MAG are funded by UNAM DGAPA PAPIIT project IA100720. MAG acknowledges support of the Spanish Ministerio de Ciencia, Innovación y Universidades grant PGC2018-102184-B-I00, co-funded by FEDER funds. GR-L acknowledges support from CONACyT grant 263373 and PRODEP (Mexico). VMAGG acknowledges support from the Programa de Becas posdoctorales of DGAPA UNAM. This work makes use of IRAF, distributed by the National Optical Astronomy Observatory, which is operated by the Association of Universities for Research in Astronomy under cooperative agreement with the National Science Foundation. This work makes use of *Herschel*, *Spitzer*, and *WISE* IR observations. *Herschel* is an ESA space observatory with science instruments provided by European-led Principal Investigator consortia and with important participation from NASA. The *Spitzer* Space Telescope was operated by the Jet Propulsion Laboratory, California Institute of Technology under a contract with NASA. Support for this work was provided by <0:funding-source 3:href="http://dx.doi.org/10.13039/100000104"/>NASA/</0:funding-source> through an award issued by JPL/Caltech. *WISE* is a joint project of the University of California (Los Angeles, USA) and the JPL/Caltech, funded by <0:funding-source 3:href="http://dx.doi.org/10.13039/100000104"/>NASA/</0:funding-source>.

DATA AVAILABILITY

The data underlying this paper will be shared on reasonable request to the corresponding author.

REFERENCES

- Arnal E. M., Cappa C. E., 1996, *MNRAS*, 279, 788
 Bailer-Jones C. A. L., Rybizki J., Fouesneau M., Mantelet G., Andrae R., 2018, *AJ*, 156, 58
 Cappa C. E., Dubner G. M., Rogers C., St-Louis N., 1996, *AJ*, 112, 1104
 Chu Y.-H., 1981, *ApJ*, 249, 195
 Chu Y.-H., Treffers R. R., Kwitter K. B., 1983, *ApJS*, 53, 937
 Cichowolski S., Duronea N. U., Suad L. A., Reynoso E. M., Noriega-Crespo A., Bronfman L., 2020, *MNRAS*, 495, 417
 Cox N. L. J. et al., 2012, *A&A*, 537, A35
 Dharmawardena T. E. et al., 2020, *ApJ*, 897, L9
 Draine B. T., 2003, *ARA&A*, 41, 241
 Ekström S. et al., 2012, *A&A*, 537, A146
 Eldridge J. J. et al., 2017, *PASA*, 34, e058
 Esteban C., Vilchez J. M., 1992, *ApJ*, 390, 536
 Esteban C. et al., 1993, *A&A*, 272, 299
 Esteban C., Mesa-Delgado A., Morisset C., García-Rojas J., 2016, *MNRAS*, 460, 4038 (E16)
 Fang X. et al., 2016, *ApJ*, 822, L19
 Fang X. et al., 2018, *ApJ*, 859, 92
 Ferland G. J. et al., 2017, *Rev. Mex. Astron. Astrofis.*, 53, 385
 Fernández-Martín A., Martín-Gordón D., Vilchez J. M., Pérez Montero E., Riera A., Sánchez S. F., 2012, *A&A*, 541, A119
 Freyer T., Hensler G., Yorke H. W., 2006, *ApJ*, 638, 262
 Fullard A. G., St-Louis N., Moffat A. F. J., Piirola V. E., Manset N., Hoffman J. L., 2020, *AJ*, 159, 214
 Garcia-Segura G., Mac Low M.-M., 1995, *ApJ*, 455, 145
 Garcia-Segura G., Langer N., Mac Low M.-M., 1996, *A&A*, 316, 133
 Götzberg Y., de Mink S. E., Groh J. H., Kupfer T., Crowther P. A., Zapartas E., Renzo M., 2018, *A&A*, 615, A78
 Gräfener G., Vink J. S., Harries T. J., Langer N., 2012, *A&A*, 547, A83
 Groenewegen M. A. T. et al., 2011, *A&A*, 526, A162
 Gruendl R. A., Chu Y.-H., Dunne B. C., Points S. D., 2000, *AJ*, 120, 2670
 Gruendl R. A., Chu Y.-H., Guerrero M. A., 2004, *ApJ*, 617, L127
 Gvaramadze V. V., Kniazev A. Y., Fabrika S., 2010, *MNRAS*, 405, 1047
 Hamann W.-R., Gräfener G., 2004, *A&A*, 427, 697
 Hamann W.-R., Gräfener G., Liermann A., 2006, *A&A*, 457, 1015
 Hamann W.-R. et al., 2019, *A&A*, 625, A57
 Houck J. R. et al., 2004, *SPIE*, 62, 5487
 Ivanova N., 2011, *ApJ*, 730, 76
 Jiménez-Hernández P., Arthur S. J., Toalá J. A., 2020, *MNRAS*, 497, 4128 (Paper I)
 Jones A. P., Tielens A. G. G. M., Hollenbach D. J., 1996, *ApJ*, 469, 740
 Juvela M., Montillaud J., Ysard N., Lunttila T., 2013, *A&A*, 556, A63
 Kochanek C. S., 2011, *ApJ*, 743, 73
 Kwitter K. B., 1981, *ApJ*, 245, 154
 Lü G., Zhu C., Podsiadlowski P., 2013, *ApJ*, 768, 193
 Luridiana V., Morisset C., Shaw R. A., 2015, *A&A*, 573, A42
 Marchenko S. V., Moffat A. F. J., Vacca W. D., Côté S., Doyon R., 2002, *ApJ*, 565, L59
 Marston A. P., 1991, *ApJ*, 366, 181
 Marston A. P., 1995a, *AJ*, 109, 1839
 Marston A. P., 1995b, *AJ*, 109, 2257
 Marston A. P., 1996, *AJ*, 112, 2828
 Marston A. P., Meaburn J., 1988, *MNRAS*, 235, 391
 Marston A. P., Welzmiller J., Bransford M. A., Black J. H., Bergman P., 1999, *ApJ*, 518, 769
 Mason B. D., Hartkopf W. I., Gies D. R., Henry T. J., Helsel J. W., 2009, *AJ*, 137, 3358
 Mata H. et al., 2016, *MNRAS*, 459, 841
 Mathis J. S., Rumpl W., Nordsieck K. H., 1977, *ApJ*, 217, 425
 Mathis J. S., Cassinelli J. P., van der Hucht K. A., Prusti T., Wesselius P. R., Williams P. M., 1992, *ApJ*, 384, 197
 Méndez-Delgado J. E., Esteban C., García-Rojas J., Arellano-Córdova K. Z., Valerdi M., 2020, *MNRAS*, 496, 2726
 Mesa-Delgado A., Esteban C., García-Rojas J., Reyes-Pérez J., Morisset C., Bresolin F., 2014, *ApJ*, 785, 100 (MD14)
 Moore B. D., Hester J. J., Scowen P. A., 2000, *AJ*, 119, 2991
 Morisset C., 2013, Astrophysics Source Code Library, record ascl:1304.020
 Morris P. W. et al., 2017, *ApJ*, 842, 79
 Ostrovskii A. B., Parfenov S. Y., Vasyunin A. I., Ivlev A. V., Sokolova V. A., 2020, *MNRAS*, 495, 4314
 Reyes-Pérez J., Morisset C., Peña M., Mesa-Delgado A., 2015, *MNRAS*, 452, 1764 (RP15)

- Sana H. et al., 2012, *Science*, 337, 444
 Scicluna P., Siebenmorgen R., Wesson R., Blommaert J. A. D. L., Kasper M., Voshchinnikov N. V., Wolf S., 2015, *A&A*, 584, L10
 Slavin J. D., Jones A. P., Tielens A. G. G. M., 2004, *ApJ*, 614, 796
 Smith J. D. T. et al., 2007a, *PASP*, 119, 1133
 Smith J. D. T. et al., 2007b, *ApJ*, 656, 770
 St-Louis N., Doyon R., Chagnon F., Nadeau D., 1998, *AJ*, 115, 2475
 Stock D. J., Barlow M. J., 2010, *MNRAS*, 409, 1429
 Stock D. J., Barlow M. J., 2014, *MNRAS*, 441, 3065
 Toalá J. A., Arthur S. J., 2011, *ApJ*, 737, 100
 Toalá J. A., Guerrero M. A., Chu Y.-H., Gruendl R. A., Arthur S. J., Smith R. C., Snowden S. L., 2012, *ApJ*, 755, 77
 Toalá J. A., Guerrero M. A., Gruendl R. A., Chu Y.-H., 2014, *AJ*, 147, 30
 Toalá J. A., Guerrero M. A., Ramos-Larios G., Guzmán V., 2015, *A&A*, 578, A66
 Toalá J. A., Guerrero M. A., Chu Y.-H., Arthur S. J., Tafoya D., Gruendl R. A., 2016, *MNRAS*, 456, 4305
 Toalá J. A., Marston A. P., Guerrero M. A., Chu Y.-H., Gruendl R. A., 2017, *ApJ*, 846, 76
 Toalá J. A., Ramos-Larios G., Guerrero M. A., Todt H., 2019, *MNRAS*, 485, 3360
 Tody D., 1993, ASP Conf. Ser. Vol. 50, Astronomical Data Analysis Software and Systems II. Astron. Soc. Pac., San Francisco, p. 173
 Tuthill P. G., Monnier J. D., Danchi W. C., 1999, *Nature*, 398, 487
 Vamvatira-Nakou C., Hutsemékers D., Royer P., Waelkens C., Groenewegen M. A. T., Barlow M. J., 2016, *A&A*, 588, A92
 van Buren D., McCray R., 1988, *ApJ*, 329, L93
 Verhoelst T., van der Zypen N., Hony S., Decin L., Cami J., Eriksson K., 2009, *A&A*, 498, 127
 Wachter S., Mauerhan J. C., Van Dyk S. D., Hoard D. W., Kafka S., Morris P. W., 2010, *AJ*, 139, 2330
 Weis K., 2001, *Rev. Mod. Astron.*, 14, 261
 Wendker H. J., Smith L. F., Israel F. P., Habing H. J., Dickel H. R., 1975, *A&A*, 42, 173

- Woitke P., Dominik C., Sedlmayr E., 1993, *A&A*, 274, 451
 Wrigge M., Chu Y.-H., Magnier E. A., Wendker H. J., 2005, *ApJ*, 633, 248

APPENDIX: DUST DESTRUCTION AT THE EDGE OF NGC 6888

To further illustrate the correlation between the gap region surrounding NGC 6888 detected in IR images and that of the nebular emission, we have created close-up, grey-scale images of the optical [O III] and that of the *Herschel* PACS 70 μm of the NE region. The images presented in Fig. A1 show with red arrows the position of the [O III] emission.

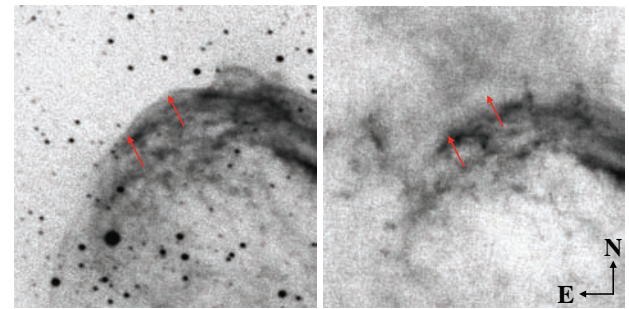


Figure A1. Close-up of the NE cap of NGC 6888. Grey scale images of the optical [O III] narrow-band filter (left-hand panel) and the *Herschel* PACS 70 μm (right-hand panel) showing the gap (lack of emission) described in Section 3. The red arrows show the edge of the [O III] in both panels. Both panels have the same FoV.

This paper has been typeset from a *T_EX/L_AT_EX* file prepared by the author.